

Energy Advances

Accepted Manuscript

This article can be cited before page numbers have been issued, to do this please use: R. B. Nair, A. A. Krishnan, M. A. Aneesh Kumar, R. Sivaraj, H. Sreehari, V. C. Bose, M. Ameen Sha, T. Matthew, S. Kurian and P. S. Arun, *Energy Adv.*, 2024, DOI: 10.1039/D4YA00463A.



This is an Accepted Manuscript, which has been through the Royal Society of Chemistry peer review process and has been accepted for publication.

Accepted Manuscripts are published online shortly after acceptance, before technical editing, formatting and proof reading. Using this free service, authors can make their results available to the community, in citable form, before we publish the edited article. We will replace this Accepted Manuscript with the edited and formatted Advance Article as soon as it is available.

You can find more information about Accepted Manuscripts in the [Information for Authors](#).

Please note that technical editing may introduce minor changes to the text and/or graphics, which may alter content. The journal's standard [Terms & Conditions](#) and the [Ethical guidelines](#) still apply. In no event shall the Royal Society of Chemistry be held responsible for any errors or omissions in this Accepted Manuscript or any consequences arising from the use of any information it contains.

ARTICLE

Ag-NiP Deposited Green Carbon Channels Embedded NiP Panels for Sustainable Water Splitting

Revathy B. Nair^a, A. Anantha Krishnan^b, Aneesh Kumar M. A.^b, Sivaraj Rajendran.^b, Sreehari Harikumar^b, Vidhya C.^c M. Ameen Sha^c, Thomas Mathew^b Sajith Kurian^{a*}, P. S. Arun^{b*}Received 00th January 20xx,
Accepted 00th January 20xx

DOI: 10.1039/x0xx00000x

Ag-NiP-deposited carbon channels on NiP panels were successfully developed through lemon juice extract (Ag-CL/NiP) and citric acid (Ag-CC/NiP)-assisted methodologies. The methods involved the precise execution of electroless deposition of the advanced Ag-Carbon matrix with NiP. The lemon juice-assisted method produced carbon channels with a dense concentration of Ag-NiP on the electrode surface, whereas the citric acid method resulted in a less dense deposition of Ag-NiP on the electrode surface, as observed from FE-SEM. The Ag-CL/NiP has remarkably higher electro- and photocatalytic water splitting performance due to the compact and conductive Ag-NiP connected with carbon channels. Electrochemical impedance analysis of Ag-CL/NiP revealed a low Rct of 491.3 Ω at the open circuit potential, indicating enhanced conductivity. The electrocatalytic Oxygen Evolution Reaction (OER) overpotential of Ag-CL/NiP was 401 mV to achieve a current density of 50 mA cm⁻², with a Tafel slope of 46.5 mV.dec⁻¹. The panel exhibited good stability, with a proven durability of over 1000 cycles of CV during OER. The developed panel achieved an impressive photo current density of ~9.5 mA cm⁻² at 1.37 V vs. RHE when subjected to light irradiation with a wavelength exceeding 420 nm. Furthermore, the Ag-CL/NiP panel demonstrated the ability to generate 17.5 mmol cm⁻² of H₂ over a 4-hour sunlight irradiation period. The temperature-controlled photocatalytic water splitting experiment revealed that the panel maintained its activity at temperatures as low as ~12°C, but with a 40% drop in efficiency compared to normal sunlight conditions

Introduction

The global economy is turning its attention to the significance of hydrogen and its associated technologies, driven by the pressing need for cleaner fuel sources and raw materials in today's world. On a global scale, there is a growing imperative to promote and scale up the green methods of hydrogen production, from the catalytic splitting of water.^{1–7} Nickel (Ni)-based materials have garnered substantial attention from both researchers and industrialists as a viable substitute for noble metals in catalytic applications, particularly in photocatalytic and electro catalytic water splitting processes. This is primarily due to their ability to achieve a high charge separation rate for photo-induced electrons and holes.^{8,9} It can serve as an efficient trapping site for capturing photo-induced electrons, thereby enhancing the effectiveness of water splitting.¹⁰ Further, the presence of NiP sites not only functions as electron probes at the solid-liquid interface but also reduces the energy barrier height for electron transfer during the water splitting process.¹¹

In certain nanocomposite systems, NiP acts as an electron carrier, promoting significant increases in the separation of interfacial charge carriers. This, further extends the lifespan of photogenerated charge carriers.^{12–16} These advantageous electronic and chemical properties establish NiP as a promising candidate for electrochemical water splitting processes.^{17,18} The widespread adoption of catalysts doped with noble metals, such as Pt, Pd, Au, and Ag, represents an effective strategy for enhancing the water splitting reaction. This is primarily attributed to the formation of highly conductive Schottky heterojunctions by these noble metals, which in turn promotes the efficient generation and separation of charge carriers.^{19,20} Additionally, metals like Au and Ag exhibit the surface plasmon resonance (SPR) effect, further augmenting the efficiency of charge transfer kinetics of photogenerated electron-hole pairs during photocatalytic reactions.^{21,22} In the pursuit of highly efficient photo/electrocatalytic water splitting processes, researchers have already explored systems incorporating silver nanoparticles. It has been documented that the integration of silver nanoparticles into catalytic systems holds promise for achieving remarkable catalytic activity.^{23–25} Notably, when silver is introduced as a dopant into nickel-based catalyst systems, it facilitates rapid electron transfer and promotes the formation of active NiOOH intermediates. Consequently, this Ag-Ni bimetallic system accelerates the rate of electrocatalytic reactions, particularly in the context of the oxygen evolution reaction (OER).²⁶ Through theoretical investigations, it has

^a Department of Chemistry, Mar Ivanios College (Affiliated to University of Kerala), Nalanchira, Thiruvananthapuram, Kerala - 695015, India.

^b Department of Chemistry, St. John's College (Affiliated to University of Kerala), Anchal, Kollam, Kerala - 691306, India.

^c Department of Applied and Environmental Chemistry, University of Szeged, Szeged, 6720, Hungary.

Electronic Supplementary Information (ESI) available.. See DOI: 10.1039/x0xx00000x



come to light that the interplay of multiple components, particularly Ag and Ni, leads to synergistic effects that significantly boost the electrocatalytic performance during the OER. These effects are attributed to several factors, including the reduction of interfacial charge transfer resistance, the optimal adsorption energy for OER intermediates, and the reinforcement of Ni-O bonding.²⁷ This synergistic interaction between Ni and Ag not only influences the electrocatalytic OER but also facilitates bulk charge separation, promoting the transfer of electron density between Ag and Ni during the electrocatalytic water reduction process.^{28,29}

Recently, there has been a growing interest in utilizing transition metals in conjunction with carbon-based materials as highly effective photo and electro catalysts for the water splitting reaction.^{30–34} Notably, the introduction of single-atom silver onto carbon in Ni-based systems has proven to enhance OER performance. This enhancement is attributed to the presence of Ag on the Ni site, which elevates the valency of Ni and subsequently reduces the adsorption energy of oxygen-containing intermediates on the active Ni sites, ultimately leading to improved OER performance.^{35,36} When considering carbon-based materials, such as graphitic carbon nitride, carbon nanotubes, and graphene have been explored as active catalysts.^{37–45} Their appeal lies in their ability to rapidly separate and transport photogenerated charge carriers, possess a high surface area, and exhibit a strong visible light harvesting capabilities. It has been reported that single-atom Ni, accompanied by a neighboring carbon atom, offers active sites for the overall water splitting reaction under visible light irradiation.^{46,47} Incorporating carbon-covered NiP into the catalyst system has demonstrated the capacity to selectively attract and extract photoinduced electrons for the water reduction process, primarily through the formation of heterojunctions.^{48–50} The distinctive morphology of the carbon component within the NiP catalyst further enhances the availability of active sites, reducing charge transfer resistance and ultimately leading to improved and stable hydrogen evolution performance.⁵¹ The combination of Ni with amorphous carbon has been documented as exhibiting remarkable performance in electrocatalytic water splitting.^{52,53} Furthermore, the utilization of a Ni-Ag bimetallic system supported on various carbon structures has shown promise as an effective choice for electrocatalytic oxidation and reduction processes.^{54,55} Recent reports have highlighted the efficacy of lemon juice-based green approaches as effective reducing agents and capping agents in the synthesis of catalytically active nanoparticles and optically active carbon quantum dots.^{56–61}

In this context, we developed highly conductive green carbon channels by utilizing lemon juice extract as both the carbon source and reducing agent. To boost their activity, these channels are further deposited with Ag-NiP, drawing inspiration from the excellent water-splitting performance of the Ag-Ni bimetallic system. This led us to propose Ag-NiP covered green carbon channels on NiP panels for enhanced electrocatalytic OER and photocatalytic Hydrogen Evolution Reaction (HER). For comparison, Ag-NiP decorated carbon channels using citric acid was also developed. Surprisingly, the lemon juice-assisted

methodology yielded a dense Ag-NiP, covered with carbon channel on the electrode surface. The system exhibited a low overpotential of 401 mV to achieve a high current density of 50 mA cm⁻², with a low Tafel slope of 46.5 mV/dec. Further, a remarkable photocurrent of ~9.5 mA cm⁻² at 0.35 V vs. Ag/AgCl was observed when subjected to light irradiation with a wavelength > 420 nm, whereas the citric acid-assisted panels generated only ~0.43 mA cm⁻². According to Marwat et al.,⁶² a benchmark material Sb₂Se₃ achieves a photocurrent density of 30 mA cm⁻² at a high potential of 1.0 V vs. Ag/AgCl. In comparison, the Ag-CL/NiP panel developed using lemon juice extract exhibits remarkably higher electrocatalytic and photocatalytic activity (**Table S1 and S2**) surpassing many recently explored catalysts. Temperature-controlled photocatalytic water splitting reactions were performed to analyze the effect of temperature on this reaction system. The Ag-CL/NiP panel retained its photo catalytic activity even at a lower temperature of ~12°C. The reusable Ag-CL/NiP panels demonstrated exceptional catalytic activity in both photocatalytic and electrocatalytic water splitting reactions. The Ag-CL/NiP panel exhibited good stability over 1000 CV cycles during the OER as well as five cycles of the photocatalytic HER. In the present work, we are introducing a highly stable and efficiently reusable catalytic system developed by exploring lemon juice-derived green panels which is capable of contributing to the growing demand for sustainable and clean energy production.

Experimental methods

Tailoring procedure of Ag-CL/NiP and Ag-CC/NiP panels

Silver-carbon powder was developed using AgNO₃ and a carbon source by the following procedure: AgNO₃ (AR grade, 1 g) was dissolved in 50 mL DI water followed by a gentle heating at 80 °C using a water bath for 10 min. A suitable amount of unprocessed lemon juice was introduced into the solution until a black color was observed. Here, lemon juice acts as the reducing agent as well as the carbon source. The solution was kept stirring at a rate of 500 rpm for a duration of 2 hours. Following this, the mixture was left undisturbed overnight at room temperature. To complete the reduction of silver ions in the solution, 0.2 mL of hydrazine (AR grade) was cautiously added drop by drop while maintaining agitation. The mixture was then subjected to stirring at 500 rpm for a period of one hour. After that, the mixture underwent filtration and several washings with DI water. The resulting residue was subjected to drying at 160 °C for 5 hours. For the comparison, a citric acid-derived silver-carbon was also developed by a similar procedure, utilizing citric acid (AR grade) as the carbon source instead of lemon juice. Both the developed Ag-carbon were deposited on NiP plate by a customized electroless deposition technique to develop the electrodes.⁶³

An electroless deposition bath was prepared by dissolving nickel sulfate (30 g L⁻¹) and succinic acid (25 g L⁻¹) in DI water. The pH of this solution was carefully adjusted and maintained between 4.5 and 5 by using NH₄OH. The temperature of the bath is



maintained at 70 °C throughout the deposition process. The reducing agent, sodium hypophosphite (25 g L⁻¹) was added, along with 100 mg of as-prepared silver-carbon powder. The pre-treated Cu plates were dipped into the bath by fixing it in vertical manner. The deposition was carried out for 90 minutes with stirring (500 rpm) and heating (70 °C). The NiP coating with silver-carbon developed using lemon juice extract and citric acid are labelled as Ag-CL/NiP and Ag-CC/NiP respectively. The schematic representation of the fabrication of Ag-CL/NiP panels is shown in **Figure 1**.

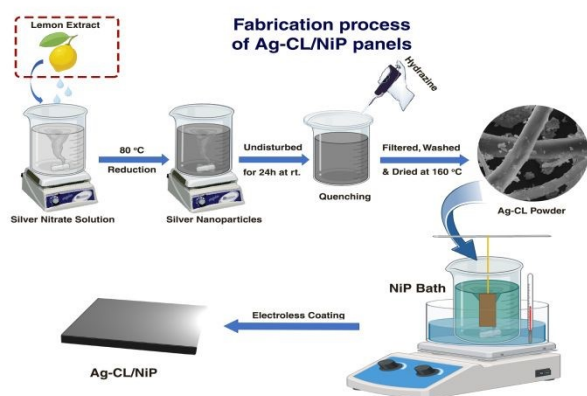


Figure 1: Scheme indicating the fabrication sequence leading to the formation of Ag-CL/NiP panels.

Physico-chemical characterizations

The developed systems were characterized using different techniques in order to unfold their material characteristics. The XRD was carried out using the Bruker D8 Advance Twin-Twin Spectrometer. UV-vis spectroscopic analysis using a ThermoScientific Nicolet iS50 - Cary 5000 high performance UV-Vis-NIR spectrophotometer, XPS analysis using Thermo Scientific ECSALAB Xi+ photoelectron spectrometer with Al K α (1486.6 eV) X-ray source were conducted. The binding energy obtained was corrected with carbon 1s (284.6 eV) reference. The SEM/EDAX analyses with Carl Zeiss EVO 18 research and FE-SEM/EDAX analysis with Carl Zeiss-Sigma 300 were performed.

Electrochemical characterization and OER efficiency analysis

All the electrochemical characterizations and OER performance were carried out using an electrochemical workstation (CH16041E USA) and the IR corrected values are reported. The electrochemical characteristics and reaction kinetics of the developed panel were analyzed by Electrochemical Impedance Spectroscopy (EIS) analysis performed in a 1 M NaOH solution at the open circuit potential (OCP) between an AC frequency range of 1 Hz to 10 KHz. Electrochemically active surface area (ECSA) was analyzed by conducting CV analysis in the non-faradaic region at different scan rates. The OER performance of the developed panels was demonstrated using cyclic voltametric analysis at a scan rate of 10 mV.s⁻¹ in 1M NaOH. LSV analysis was conducted to calculate the OER overpotential at a

scan rate of 10 mV.s⁻¹. The electrochemical stability during OER was confirmed by linear sweep voltametric analysis before and after conducting 1000 cycles of CV. The electrochemical characteristics and OER performance were evaluated using three electrodes set up with a Pt mesh (5 cm²) as the counter electrode.

Photocatalytic water splitting analysis

The photocatalytic water splitting efficiencies of Ag-CL/NiP and Ag-CC/NiP were investigated simultaneously under natural sunlight. A surface area of 2 cm² on the developed panel was exposed to sunlight. The prepared panels were placed in 40 mL water-methanol (3:1) mixture in an airtight borosilicate round bottom flask (70 mL). Then N₂ gas was purged to the mixture for 45 minutes to provide inert atmosphere during irradiation. The variation of temperature of the reaction medium throughout the reaction was monitored. The volume of hydrogen gas generated was periodically monitored by a PerkinElmer gas chromatograph Clarus 590 with a thermal conductivity detector. The reusability of the panel was monitored under exactly the same conditions for 5 cycles. The temperature dependence on the photocatalytic activity of the catalyst was monitored at temperatures starting from -0 °C under natural sunlight, and hydrogen evolution was quantified to analyze the effect of temperature.

Results and Discussion

Deciphering the physico-chemical characteristics of the Ag-CL/Ni-P panels

The crystallographic characteristics of the Ag-carbon powder Ag-CL and Ag-CC, NiP and Ag-CL/NiP panels were examined using XRD, and the results are shown in **Figure 2(a)**. The XRD pattern evidenced the formation of crystalline Ag with cubic structure (JCPDS65-2871) in the case of both the lemon juice and citric acid assisted methods. The diffraction pattern had sharp peaks at 2 θ values of 38.2°, 44.4°, 64.6°, which can be ascribed to the features from the (111), (200), and (220) lattice planes of cubic Ag (JCPDS65-2871). The most intense plane of Ag, (111) has high density atoms and a flat, two dimensional surface making more suitable for catalytic reactions.⁶⁴ The Ag can form effective Schottky junction with NiP which can also enhance the photocatalytic water splitting performance.⁶⁴ Both the planes of NiP, (111) at around 44° and (200) around 52° were observed for in the Ag-CL/NiP panel. The efficiency of various planes in electrocatalytic activity may vary with the reaction conditions, media and materials.⁶⁵ The intense peaks of Ag were also retained after the incorporation of the Ag-carbon powder in the NiP panels. These results revealed that Ag with a cubic crystal structure is incorporated along with NiP in the Ag-CL/NiP panel via the electroless coating.

The chemical states of elements in the systems analysed using XPS and the results are shown in **Figure 2 (b-e)**. In the case of NiP, the predominant peak for Ni 2p_{3/2} was observed at 854.94 eV, and the coupling constant value was determined to be 17.46 eV, consistent with the Ni²⁺ oxidation state.⁶⁶ Conversely, in the



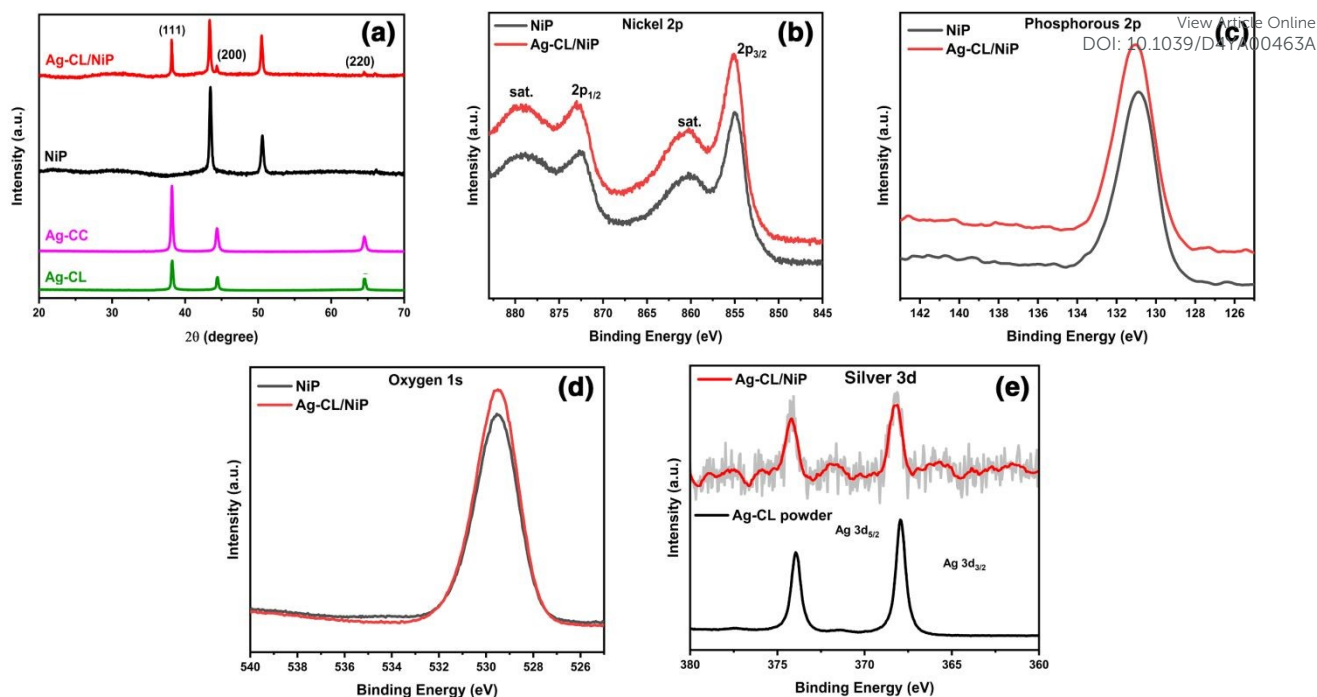


Figure 2: (a) XRD pattern of Ag-CL powder, Ag-CC powder, NiP, Ag-CL/NiP and (b - e) XPS spectra showing Ni2p, P2p, O1s and Ag3d respectively, of NiP & Ag-CL/NiP

Ag-CL/NiP system, the major peak for Ni $2p_{3/2}$ was recorded at 855.34 eV, with a coupling constant value of 17.71 eV, further

confirming the presence of the Ni^{2+} oxidation state in both NiP and Ag-CL/NiP.⁶⁶ The phosphorous $2p_{3/2}$ peaks in both NiP and Ag-CL/NiP were detected at 130.3 eV, **Figure 2 (d)**, providing evidence for the existence of elemental phosphorus ($2p_{3/2}$).⁶⁷ Also, the Ag $3d_{5/2}$ core level feature was identified at 368.2 eV, accompanied by a spin-orbit coupling constant of 6 eV, indicative of the Ag^0 oxidation state.⁶⁸ The binding energy of Ni $2p_{3/2}$ positively shifted by 0.4 eV when Ag-Carbon powder was loaded into NiP. While the binding energy of Ag $3d_{5/2}$ negatively shifted by 0.8 eV, there was no significant shift in the binding energy of phosphorus when Ag-Carbon was loaded onto NiP. There was a discernible shift in the Ag $3d_{5/2}$ peak to 367.4 eV in the case of Ag-CL/NiP, potentially suggesting electron transfer from NiP to silver.⁶⁹

The elemental composition of NiP was analyzed using EDAX and is shown in **Figure S2** of *ESI*. The EDAX analysis shows that the NiP panel consists solely of nickel and phosphorous, and the corresponding EDAX mapping is shown in **Figure S1 (e, f)** of *ESI*. In contrast, the Ag-CL/NiP panel exhibited a more complex composition, including Ag, Ni, phosphorous, and carbon, as seen in **Figure 3 (c)**. EDAX mapping of Ag-CL/NiP is shown in **Figure 4 (d-h)**. There were no indications of any other impurities, demonstrating dense coverage over the NiP surface by the developed Ag-NiP covered carbon channels.

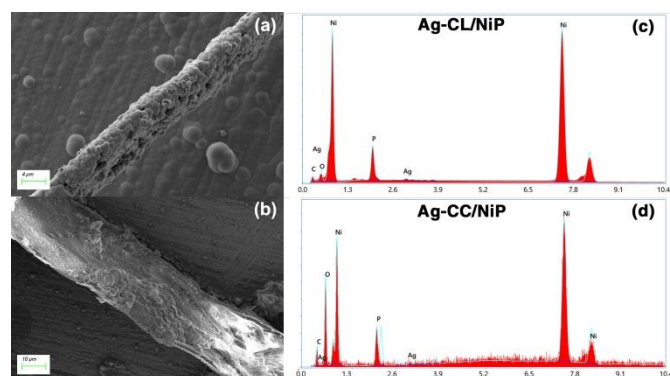


Figure 3: FE-SEM image of Ag-NiP deposited carbon channels on the surface of NiP panel (a) Ag-CL/NiP (b) Ag-CC/NiP and EDAX spectra of (c) Ag-CL/NiP (d) Ag-CC/NiP

The morphological characteristics of Ag-CL/NiP and Ag-CC/NiP were analyzed using FE-SEM and are shown in **Figure 3 (a, b)**. The FE-SEM analysis revealed the formation of channel-like structures on the NiP panels' surface, which were densely covered with Ag-NiP in Ag-CL/NiP. EDAX spectroscopy confirmed that these channels consist of nickel, phosphorous, carbon, and silver, as shown in **Figure 3 (c, d)**. The surface



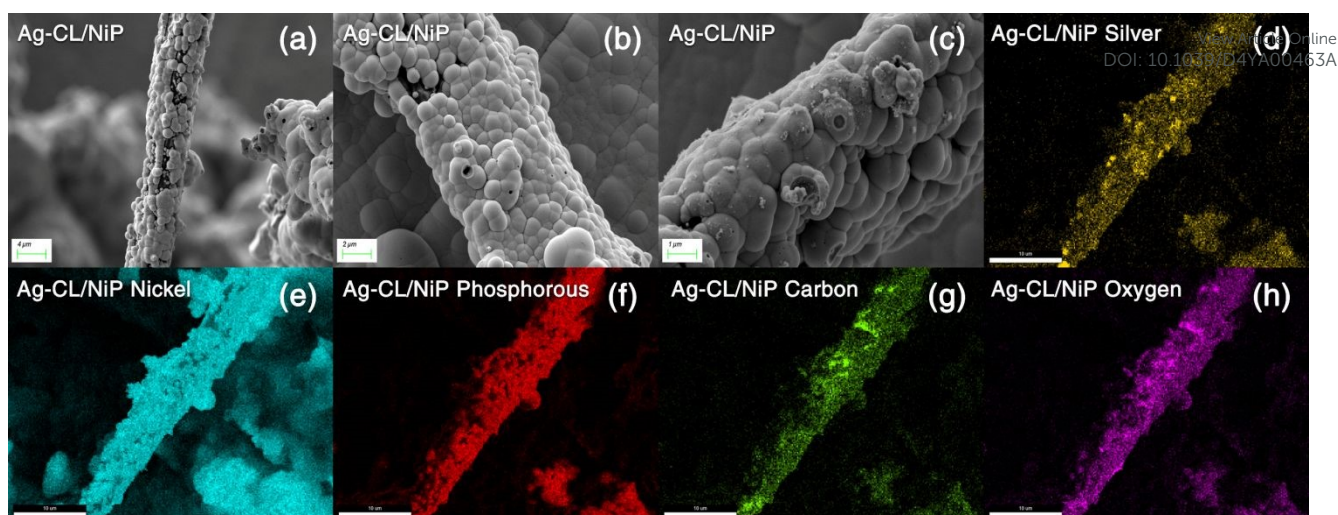


Figure 4: FE-SEM images of (a – c) Ag-CL/NiP at different magnifications and EDAX mapping of (d– h) Ag-CL/NiP panel

carbon concentration was notably higher in Ag-CC/NiP than in Ag-CL/NiP. This suggests that the lemon juice-assisted method generated carbon channels densely covered with Ag-NiP. In addition to that, the FE-SEM images and EDAX mapping shown in **Figure 4 (a–d)** and **Figure S3 (a–h)** of *ESI* also support this observation. The morphological characteristics of the Ag-carbon powder developed using lemon juice extract were also assessed through SEM analysis, and the corresponding images are presented in **Figure S1 (c, d)** of *ESI*. The SEM images and EDAX mapping show the presence of agglomerated particles intertwined with channel-like structures. Elemental mapping (**Figure S1 (g, h)** of *ESI*) confirms that these agglomerated and channel-like structures are primarily composed of a carbon framework, with silver particles adorning the carbon surfaces.

Electrochemical characteristics and active surface area analysis

EIS was employed to assess the electrical conductivity of the fabricated Ag-CL/NiP and Ag-CC/NiP and was juxtaposed with the NiP panel. The corresponding Nyquist plots at their open circuit potential are shown in **Figure 5 (a)**. The diameter of the semicircle in the Nyquist plot corresponding to the developed Ag-CL/NiP panel was notably smaller when compared to that of the Ag-CC/NiP and NiP panels in **Figure 5 (a, inset)**. This observation strongly supports the idea of enhancement of conductivity of the Ag-CL/NiP panel, signifying a prolonged lifetime for electron-hole pairs, a characteristic that augments photo- and electrocatalytic activity.

The Nyquist plots, along with the corresponding equivalent circuit used for fitting, are depicted in **Figure 5 (a)**. Notably, the charge transfer resistance (R_{ct}) value for the Ag-CL/NiP panel was measured at OCP as 491.3 Ω stands in stark contrast to the R_{ct} values obtained for the Ag-CC/NiP and NiP panels using the same circuit, which were 598.6 Ω and 55, 744 Ω respectively. Also, the analysis involved the determination of the constant phase element (Q) to establish the electrochemical performance. It's worth noting that the Q value for the developed Ag-CL/NiP panel was $2.87 \times 10^{-3} \text{ F cm}^{-2} \text{ s}^{\alpha-1}$, whereas for Ag-CC/NiP, it was lower at $2.49 \times 10^{-3} \text{ F cm}^{-2} \text{ s}^{\alpha-1}$. These

findings revealed that in Ag-CL/NiP, there was an improvement in the electrochemically active surface area, consequently enhancing the electrochemical performance of the panel.^{70,71} To confirm this observation, the ECSA of the panels was determined using the double layer capacitance method, following the approach described by Anantharaj et al.^{72,73} CV analyses of Ag-CL/NiP and Ag-CC/NiP were conducted within the non-faradaic region at various scan rates, and the corresponding graphs are shown in **Figure 5 (d–g)**, and the resulting current density was plotted against the scan rate. ECSA was calculated using the following equation:

$$\text{ECSA} = C_{dl} / C_s$$

Here, C_{dl} represents the double-layer capacitance, obtained from the slope of the current density vs. scan rate, and C_s corresponds to the specific capacitance of the electrolyte used. The C_{dl} values obtained were: 0.4724 $\mu\text{F.cm}^{-2}$ for Ag-CL/NiP, 0.2689 $\mu\text{F.cm}^{-2}$ for Ag-CC/NiP, and 0.0943 $\mu\text{F.cm}^{-2}$ for NiP. The higher C_{dl} value of Ag-CL/NiP ensures enhanced OER performance.

The ECSA value determined for the developed Ag-CL/NiP panel (11.81 cm^2) was higher than that of the Ag-CC/NiP (6.72 cm^2). These findings clearly establish that the electrocatalytically active surface area of the developed Ag-CL/NiP panels surpasses that of Ag-CC/NiP by a factor of two. These results reveal that the dense covering of carbon channels with Ag-NiP on the NiP surface enhances the electrochemically active surface area. Therefore, this dense Ag-NiP covering plays a crucial role in the electrochemical activity of Ag-CL/NiP.

Electrocatalytic oxygen evolution

The kinetics of OER catalysis and efficiency analysis of both the Ag-CL/NiP and Ag-CC/NiP panels were conducted using a three-electrode system, as outlined in the experimental section. To analyze the OER activity of the developed panels, Tafel (**Figure 5 (b)**) and LSV (**Figure 5 (c)**) analyses were performed, and the overpotential at a current density of 50 mA cm^{-2} was assessed. The Ag-CL/NiP panel exhibited an overpotential of 401 mV, which is markedly less than that of both Ag-CC/Ni-P (491 mV)



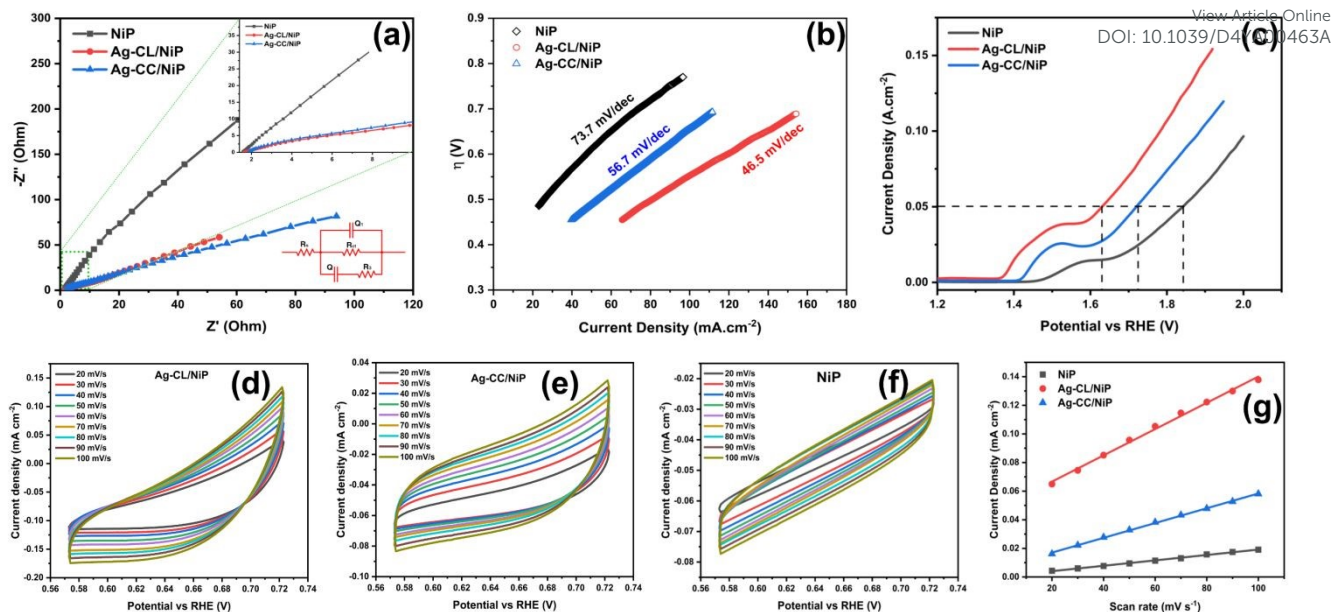


Figure 5: (a) Nyquist plot and equivalent circuit (b) Tafel curves (c) LSV curves. Analysis of the electrochemically active surface area (ECSA): CV curves of (d) Ag-CL/NiP (e) Ag-CC/NiP (f) NiP. Determination of C_{dl} using (g) the plot of double layer charging current density variation vs. scan rate by a linear regression of Ag-CL/NiP, Ag-CC/NiP and NiP.

and NiP (614 mV) to achieve the same current density. The corresponding Tafel analysis results also indicated that the Ag-CL/NiP panel possessed a Tafel slope value of 46.5 mV dec⁻¹, which was less than those of both Ag-CA/Ni-P (56.7 mV dec⁻¹) and Ni-P (73.7 mV dec⁻¹) panels. These findings confirm a substantial improvement in the OER activity kinetics attributable to the incorporation of Ag-NiP covered carbon channels within the NiP panel. The low charge transfer resistance observed at the Ag-CL/NiP electrode surface-electrolyte interface, and the high C_{dl} values suggest that this panel can be employed effectively for electrocatalytic OER.

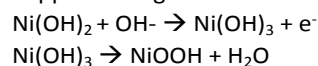
The reversible characteristics of Ag-CL/NiP panels can be observed from CV, as shown in **Figure S4** of *ESI*, provide clear evidence of the superior OER efficiency of the developed panels. The voltametric response observed before 1.4 V vs. RHE was due to Ni oxidation, as detailed in the mechanism of OER, and parallelly, the oxygen evolution was started when the current density reached 10 mA cm⁻² (**Figure S7** of *ESI*).

The reversible OER activity is clearly illustrated through CV analysis, as presented in **Figure S4** of *ESI*. The Ag-CL/NiP panels exhibit remarkable reversible OER performance, despite the OER process being inherently sluggish and requiring a high overpotential due to its demanding 4-electron process. The reversible nature can be seen by looking into the ΔE value ($\Delta E = E_{red.} - E_{ox.}$). The ΔE value for Ag-CL/NiP was 0.29 V, compared to 0.22 V for Ag-CC/NiP. The peak current (i_p) value of 63 mA cm⁻² for Ag-CL/NiP was significantly higher than that of Ag-CC/NiP (42 mA cm⁻²) and NiP (6.9 mA cm⁻²). The overall electrochemical stability was confirmed by LSV analysis conducted before and after 1000 cycles of CV (**Figure S5 and S6** of *ESI*). Only a slight shift in the LSV curve was observed after 1000 cycles of CV, indicating that the developed Ag-CL/NiP panel has exceptionally high electrocatalytic OER efficiency and stability. The results of

electrocatalytic OER performance obtained for Ag-CL/NiP are compared with recent literature reports in **Table S1** of *ESI*. These comparisons reveal that Ag-CL/NiP possess superior electrocatalytic OER efficiency compared to recently reported systems.

Electrocatalytic OER Mechanism

Drawing insights from the OER test results and a thorough examination of the developed panel's characters, a plausible mechanism for the OER process is proposed. The Ag-CL/NiP catalyst displays heightened OER activity in alkaline environments, which can be attributed to the dual-site adsorbate evolution (AEM) electron transfer mechanism. Within the Ag-CL/NiP structure, phosphorus naturally has an inclination to abstract oxygen or hydroxide species on its surface or bond covalently with O, resulting in the formation of phosphorous oxide or hydroxide.^{74,75} The presence of Ag and Ni enhances the metal sites' ability to absorb OOH* intermediates, facilitating a dual-site mechanism that promotes the OER process.^{76–78} Similarly, the XPS data of Ag-CL/NiP shows a higher binding energy Ni 2p_{3/2} peak (855.34 eV) compared to that in NiP (854.94 eV), indicating that the Ni²⁺ species are in a less electron dense state. This state is conducive to electrostatic interactions with hydroxide ions, facilitating their rapid conversion into nickel hydroxide. The reactions that might happen during OER is as follows⁷⁹,



The emergence of NiOOH is an intermediate step within the widely acknowledged OER mechanism.⁸⁰ In this context, the rapid formation of NiOOH is facilitated by the electrostatic interaction between the higher oxidation states of nickel and OH⁻ ions, effectively amplifying OER activity.^{81–83} Another



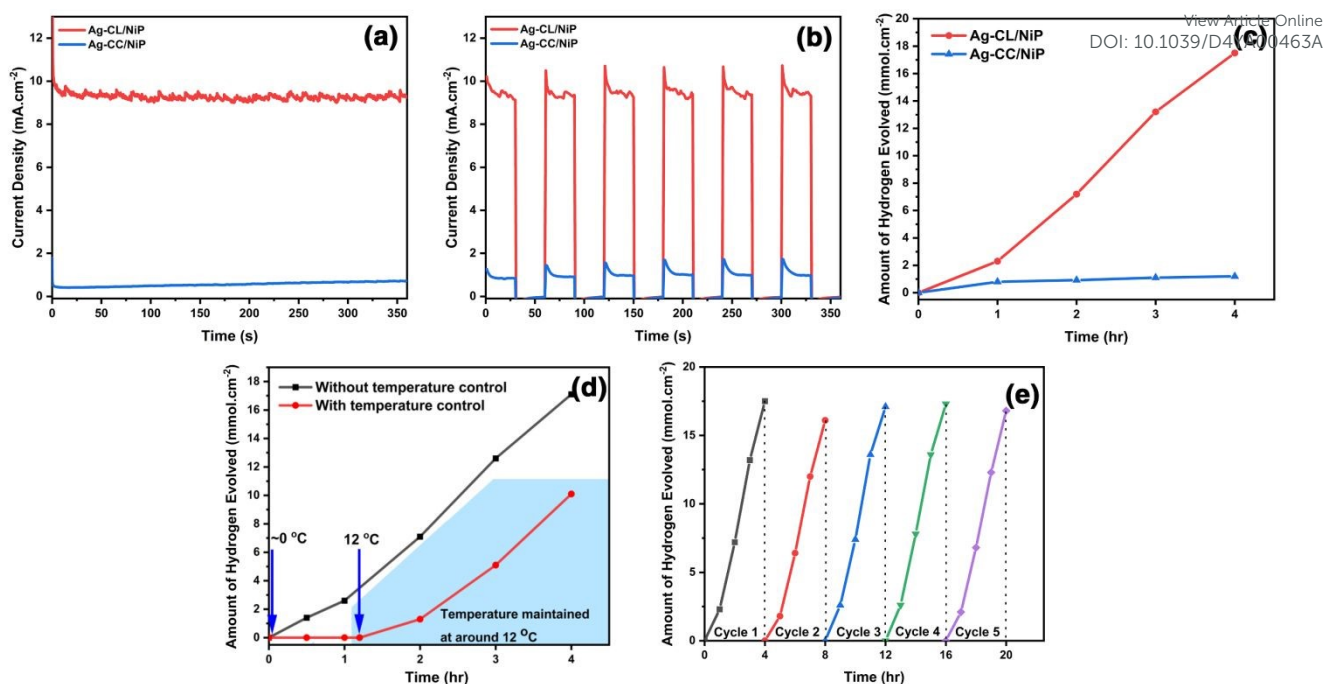


Figure 6: Photocurrent measurement (a) single step of CA (b) multistep of CA (c) Comparison of photocatalytic water splitting analysis of Ag-CL/NiP and Ag-CC/NiP (d) Temperature dependence of photocatalytic water splitting performance of Ag-CL/NiP (e) Reusability analysis of Ag-CL/NiP

pivotal factor contributing to excellent OER activity is the presence of an ample number of adsorption sites for OH⁻ during the OER process. In this particular system, apart from the Ni adsorption sites, Ag also serves as an OH adsorption site, thereby enhancing OER activity through a dual site adsorption mechanism.⁸⁴

During the adsorption process, [O*] and OH* (*denotes the adsorption site) intermediates exhibit a tendency to bind to carbon sites, while the OOH* intermediate exhibits a preference for adsorption on nickel ion sites.⁸⁵ Incorporating the heteroatom Ag into the carbon ribbon within NiP introduces additional active sites for the adsorption of OOH*, enhancing the dual site mechanism. Furthermore, Ag can act as sites for hydrogen interaction, facilitating the accumulation of protons from OOH* intermediates and the efficient release of O₂ molecules. This hydrogen abstraction from OOH* and the creation of new active sites consequently reduce the system's overpotential. The OER process with Ag-CL/NiP achieved a low overpotential of 401 mV at 50 mA cm⁻², signifying the superior performance of this panel in comparison to both Ag-CC/NiP and NiP panels. The presence of the carbon channel and the heteroatom Ag serves as an electron transport facilitator, expediting ion transport and leading to a significant reduction in the R_{ct} value, which measured at 491.3 Ω.

Photocatalytic water splitting performance

The photocatalytic performance of the developed panel was assessed by exposing a 2 cm² area of the panel, as mentioned in the experimental session. Over a 4-hour irradiation period, the Ag-CL/NiP panel demonstrated the ability to generate 17.5 mmol.cm⁻² of H₂ (Figure 6 (c)), while Ag-CC/NiP yielded only 1.2

mmol.cm⁻² of H₂. This superior photocatalytic efficiency can be attributed to the very low interfacial charge transfer resistance and the higher double layer capacitance resulting from the presence of the highly conductive Ag-NiP covered carbon channels on the surface of NiP.

To validate this observation, a photocurrent measurement was conducted using chronoamperometric analysis at 1.37 V vs. RHE, utilizing light with a wavelength exceeding 420 nm. Figure 6 (a, b) illustrates that the Ag-CL/NiP panel consistently generated a high current density of ~9.5 mA cm⁻², whether in a single-step or multi-step procedure, when exposed to light at 420 nm and 1.37 V vs. RHE. In similar analysis parameters, Ag-CC/NiP managed to produce only around 0.43 mA cm⁻² of current density. According to Marwat et al.,⁶² the benchmark materials Sb₂Se₃ and TiO₂-NR/CdS-NiO_x⁸⁶ achieved a photocurrent density of 30 mA cm⁻² at a high potential of 1.0 V vs. Ag/AgCl. Here, the Ag-CL/NiP panel only need a potential of 0.35 V vs. Ag/AgCl to provide a photocurrent of ~9.5 mA cm⁻². These findings indicate that, under light irradiation, a substantial number of electron-hole pairs are generated and efficiently transported to the surface sites due to the exceptional conductivity of Ag-CL/NiP. In contrast, the significantly lower current observed for Ag-CC/NiP underscores the crucial role played by the Ag-NiP covered carbon channels. Moreover, the method of deposition and the use of unprocessed lemon juice as a carbon source are identified as the primary contributing factors to these exceptional qualities in the Ag-CL/NiP panel.

The temperature-dependent photocatalytic activity of the Ag-CL/NiP panel was investigated under natural sunlight, with temperatures ranging from approximately 0 °C. The resulting



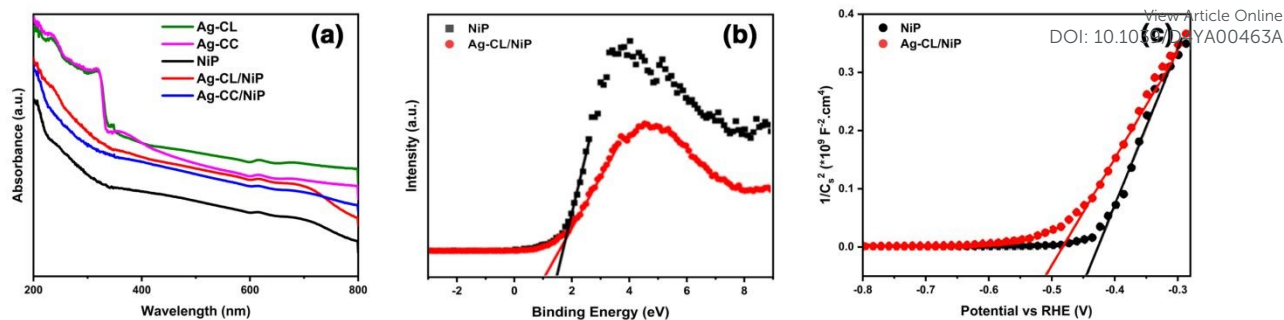


Figure 7: (a) UV-Visible diffuse reflectance spectra of NiP, Ag-CC/NiP, Ag-CL/NiP, Ag-CC powder and Ag-CL powder, (b) Valence band analysis using XPS (c) Mott-Schottky plot used to calculate conduction band

hydrogen evolution was quantified to elucidate the effects of temperature on the catalytic process, and the results are shown in **Figure 6 (d)**. Notably, gas production from water splitting with this system becomes feasible only above a critical temperature threshold of $\sim 12^\circ\text{C}$, where significant gas evolution initiates. At this temperature, the water splitting process was carried out for 4 hours, yielding a gas production rate of $10.1 \text{ mmol}\cdot\text{cm}^{-2}$. However, under natural sunlight, without temperature control, the system generated $17.1 \text{ mmol}\cdot\text{cm}^{-2}$ of gas after 4 hours, with the solution temperature varying between $\sim 33^\circ\text{C}$ and $\sim 44^\circ\text{C}$ throughout the experiment. The temperature fluctuations over time are depicted in **Figure S8** of *ESI*. These results demonstrated that when temperature was controlled to $\sim 12^\circ\text{C}$ there was $\sim 40\%$ decrement in hydrogen evolution performance which underlines the material's catalytic potential in water splitting under low temperature. The apparent quantum yield was decreased from $1.8 \times 10^{-2}\%$ to $1.04 \times 10^{-2}\%$ when temperature was reduced from RT to $\sim 12^\circ\text{C}$, as shown in *ESI*. The assessment of reusability demonstrated that the catalytic performance of the Ag-CL/NiP panel remains nearly unchanged even after undergoing five cycles of continuous water splitting, and the results are shown in **Figure 6 (e)**. Any slight variations in activity can be attributed to fluctuations in solar intensity. Importantly, these panels can be easily reused without any additional treatment. This reusability feature makes these panels readily suitable for integration into industrial water splitting processes. The results of the photocatalytic water splitting performance obtained in this study were compared to those of notable systems reported in the literature, as shown in **Table S2** of *ESI*. These comparisons reveal that the current system exhibits superior photocatalytic efficiency.

Electron transfer mechanism in photocatalysis

A plausible electron transfer mechanism in Ag-CL/NiP is demonstrated with the SPR effect of noble Ag nanoparticles. Besides the SPR effect of Ag, a Schottky barrier and synergism is developed between Ag and NiP on the green carbon channels. The UV-visible diffuse reflectance spectra shown in **Figure 7 (a)** clearly demonstrate that the synthesized Ag-CL and Ag-CC powder particles have characteristic absorption in the UV-visible region. It is also evident that the synthesized NiP exhibited a characteristic absorption in the UV-visible region;

however, in the Ag-CL/NiP, the intensity of the absorption band in the UV-visible region significantly increased due to Ag-CL powder incorporation. These results imply that Ag-CL/NiP is able to absorb the entire UV-visible region of the spectra. Moreover, XPS analysis provided insights into the valence band of the developed panels, as depicted in **Figure 7 (b)**. The valence band for NiP was 1.6 eV, while for Ag-CL/NiP it was 1.2 eV. A significant reduction in the valence band position was observed in the case of Ag-CL/NiP. This shift can be attributed to the effective overlap of Ni and Ag orbitals facilitated by the carbon channels derived from lemon juice, as shown in **Figure 7 (b)**. This observation can be attributed to the synergistic interaction between Ni and Ag.⁸⁷

The determination of the conduction band position for the panels was carried out through Mott-Schottky analysis under dark conditions at 1 KHz (**Figure 7 (c)**). Specifically, for NiP, the conduction band was identified at -0.43 eV , while for Ag-CL/NiP, it was positioned at -0.5 eV . This shift is attributed to the fermi level equilibration between Ag and NiP, facilitating a smooth electron transfer from Ag to NiP.⁸⁸ The calculated band gap values for Ag-CL/NiP and NiP were found to be 1.7 eV and 2.03 eV, respectively. These findings indicate a substantial reduction in the bandgap upon incorporating Ag-CL powder into the NiP panel. This decrease can be attributed to the robust overlap between the orbitals of Ni and Ag. As reported by XPS data, the

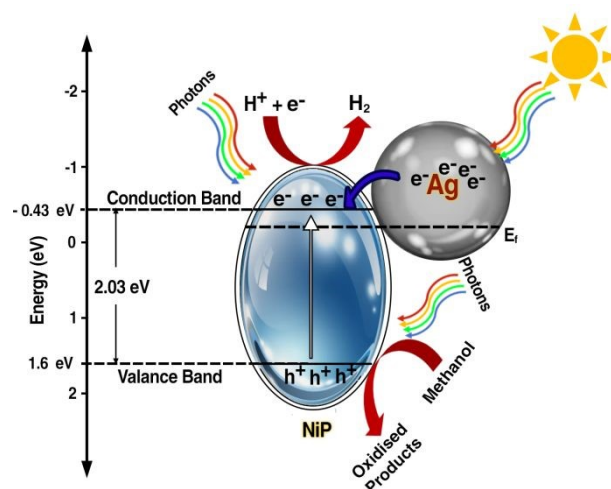


Figure 8: Plausible photocatalytic water splitting mechanism of Ag-CL/Ni-P.



binding energy of Ni 2p_{3/2} shifted to the positive region by 0.6 eV, while the binding energy of Ag shifted to the negative region by 0.8 eV. These results point to the migration of electrons from Ni to Ag alongside the migration of electron from nickel to phosphorous indicating a synergic effect between Ni and Ag. A plausible mechanism for Ag-CL/NiP is depicted in **Figure 8**.

Under the irradiation of sunlight, electron excitation takes place simultaneously in both electron rich Ag and in NiP in Ag-CL/NiP. An electron shuttling occurs through the conductive carbon channels. Due to the SPR effect of Ag, the electron-hole generation is enhanced. The photo-generated electron migrates from CB of Ag to CB of NiP through the green carbon channel which also facilitates the smooth electron transfer process. Ag forms Schottky barriers at the interface, which prevents the electrons and holes recombination by generating an energy barrier that the electrons must overcome to recombine with holes, thus prolonging the lifetime of charge carriers. However, hydrogen reduction cannot occur at the surface of Ag due to weak bond strength between Ag and H (Ag-H).⁸⁷ Therefore, at the CB position of Ni-P, H⁺ ions are reduced to generate H₂ gas. The holes were gathered on VB of NiP and oxidized the methanol to useful organic compounds.

Conclusions

Ag-NiP deposited green carbon channels embedded NiP panels were developed using lemon juice extract and precise execution of electroless NiP coating for sustainable electro- and photocatalytic water splitting processes. The lemon juice-assisted methodology yielded a compact Ag-NiP, with green carbon channels on the electrode surface. The Ag-CL/NiP displayed reversible OER kinetics with a low overpotential of 401 mV to achieve a current density of 50 mA cm⁻². It displayed a Tafel slope of 46.5 mV.dec⁻¹ and followed the dual-site Adsorbate Evolution Mechanism. The Ag-CL/NiP achieved a photocurrent density of ~9.5 mA cm⁻² at a lower voltage of 0.35 V vs. Ag/AgCl when subjected to light irradiation with a wavelength > 420 nm. Under 4 hours of sunlight irradiation, the Ag-CL/NiP panel achieved a hydrogen production rate of 17.5 mmol cm⁻², demonstrating its impressive capacity for solar-driven H₂ generation. Temperature-controlled photocatalytic water splitting was conducted and the system exhibited a reasonable performance (~40% lower compared to that at normal sunlight conditions) at a lower temperature of 12 °C. These easily reusable high-performance Ag-CL/NiP panels promise its effective incorporation in industrial water splitting process for carbon-neutral hydrogen production.

Author Contributions

The manuscript was written through contributions of all authors. All authors have given approval to the final version of the manuscript. All authors contributed equally.

Conflicts of interest

There are no conflicts to declare.

View Article Online
DOI: 10.1039/D4YA00463A

Data availability

Data will be available on request.

Acknowledgements

The authors gratefully acknowledge DST, New Delhi, for the facility support under DST-FIST programme in St. John's College, Anchal, Kerala, India. R.B.N, A.A.K and S.H. thank University of Kerala for research fellowships. S.R., and V.C. thank UGC for research fellowships.

We gratefully acknowledge CLIF, Kerala University, STIC Kochi and Material Characterization FESEM Lab, Bannari Amman Institute of Technology for providing material analysis data.

References

- 1 B. Tam, O. Babacan, A. Kafizas and J. Nelson, *Energy Environ. Sci.*, 2024, **17**, 1677–1694.
- 2 L. Zhao, Z. Lv, Y. Shi, S. Zhou, Y. Liu, J. Han, Q. Zhang, J. Lai and L. Wang, *Energy Environ. Sci.*, 2024, **17**, 770–779.
- 3 E. Boivin, S. Saitzek, F. Fauth, M. Huvé, P. Roussel and H. Kabbour, *Chem. Mater.*, 2022, **35**, 447–456.
- 4 C. Avcioglu, S. Avcioglu, M. F. Bekheet and A. Gurlo, *ACS Appl. Energy Mater.*, 2023, **6**, 1134–1154.
- 5 H. Jiao, C. Wang, L. Xiong and J. Tang, *Accounts Mater. Res.*, 2022, **3**, 1206–1219.
- 6 R. V. Digraskar, B. B. Mulik, P. S. Walke, A. V. Ghule and B. R. Sathe, *Appl. Surf. Sci.*, 2017, **412**, 475–481.
- 7 H. Gunaseelan, A. V. Munde, R. Patel and B. R. Sathe, *Mater. Today Sustain.*, 2023, **22**, 100371.
- 8 X. Yan, M. Xia, H. Liu, B. Zhang, C. Chang, L. Wang and G. Yang, *Nat. Commun.* 2023 141, 2023, **14**, 1–11.
- 9 Y. Zhao, W. Xue, W. Sun, H. Chen, X. Li, X. Zu, S. Li and X. Xiang, *Int. J. Hydrogen Energy*, 2023, **48**, 31161–31171.
- 10 Y. Xiao, Z. Wang, L. Li, Q. Gu, M. Xu, L. Zhu and X. Fu, *Int. J. Hydrogen Energy*, 2023, **48**, 15460–15472.
- 11 G. Jia, M. Sun, Y. Wang, X. Cui, B. Huang and J. C. Yu, *Adv. Funct. Mater.*, 2023, **33**, 2212051.
- 12 A. Chouat, D. T. Nguyen, S. Mohan and T. O. Do, *ACS Appl. Nano Mater.*, 2022, **5**, 13078–13089.
- 13 W. Ma, D. Zheng, B. Xiao, Y. Xian, Q. Zhang, S. Wang, J. Liu, P. Wang and X. Hu, *J. Environ. Chem. Eng.*, 2022, **10**, 107822.
- 14 Y. Wu, Y. Li, L. Zhang and Z. Jin, *ChemCatChem*, 2022, **14**, e202101656.
- 15 L. Wei, M. A. S. Adamson and J. Vela, *ChemNanoMat*, 2020, **6**, 1179–1185.
- 16 F. Li, C. Liu, H. Lin, Y. Sun, H. Yu, S. Xue, J. Cao, X. Jia and S. Chen, *J. Colloid Interface Sci.*, 2023, **640**, 329–337.
- 17 M. Wang, L. Zhou, M. Zhang, W. Song, W. Zhong, X. Wang and Y. Tang, *ChemistrySelect*, 2022, **7**, e202202462.
- 18 J. Nie, J. Shi, T. Huang, M. Y. Xie, Z. Y. Ouyang, M. H. Xian, G. F. Huang, H. Wan, W. Hu and W. Q. Huang, *Adv. Funct. Mater.*, 2024, **34**, 2314172.



- 19 T. N. Q. Trang, T. B. Phan, N. D. Nam and V. T. H. Thu, *ACS Appl. Mater. Interfaces*, 2020, **12**, 12195–12206.
- 20 L. Li, Q. Zhang, X. Wang, J. Zhang, H. Gu and W. L. Dai, *J. Phys. Chem. C*, 2021, **125**, 10964–10973.
- 21 D. Gelija, C. Loka, M. Goddati, N. H. Bak, J. Lee and M. D. Kim, *ACS Appl. Mater. Interfaces*, 2023, **15**, 34883–34894.
- 22 H. Qiu, A. Yamamoto and H. Yoshida, *ACS Catal.*, 2023, **13**, 3618–3626.
- 23 F. Naaz and T. Ahmad, *Langmuir*, 2023, **39**, 9300–9314.
- 24 R. K. Sharma, S. Yadav, S. Dutta, H. B. Kale, I. R. Warkad, R. Zboril, R. S. Varma and M. B. Gawande, *Chem. Soc. Rev.*, 2021, **50**, 11293–11380.
- 25 D. Li, Y. Qin, J. Liu, H. Zhao, Z. Sun, G. Chen, D. Y. Wu, Y. Su, S. Ding and C. Xiao, *Adv. Funct. Mater.*, 2022, **32**, 2107056.
- 26 H. Zhang, H. Tang, Q. Weng, Q. Wei, M. Duan, X. Bo, F. Fu and L. Zan, *J. Solid State Chem.*, 2022, **316**, 123556.
- 27 F. Wang, Y. Zhang, J. Zhang, W. Yuan, Y. Li, J. Mao, C. Liu, C. Chen, H. Liu and S. Zheng, *ACS Sustain. Chem. Eng.*, 2022, **10**, 5976–5985.
- 28 T. Xu, J. Wang, M. Wang, Y. Xue, J. Liu, N. Cai, W. Chen, F. Huang, X. Li and F. Yu, *New J. Chem.*, 2021, **45**, 13286–13292.
- 29 Y. Hu, Y. Wu, J. Feng, H. Huang, C. Zhang, Q. Qian, T. Fang, J. Xu, P. Wang, Z. Li and Z. Zou, *J. Mater. Chem. A*, 2018, **6**, 2568–2576.
- 30 A. T. Hoang, A. Pandey, W. H. Chen, S. F. Ahmed, S. Nizetić, K. H. Ng, Z. Said, X. Q. Duong, Ü. Ağbulut, H. Hadiyanto and X. P. Nguyen, *ACS Sustain. Chem. Eng.*, 2023, **11**, 1221–1252.
- 31 S. S. Narwade, B. B. Mulik, S. M. Mali and B. R. Sathe, *Appl. Surf. Sci.*, 2017, **396**, 939–944.
- 32 R. V. Digraskar, V. S. Sapner, S. M. Mali, S. S. Narwade, A. V. Ghule and B. R. Sathe, *ACS Omega*, 2019, **4**, 7650–7657.
- 33 S. S. Narwade, S. M. Mali, V. S. Sapner and B. R. Sathe, *ACS Appl. Nano Mater.*, 2020, **3**, 12288–12296.
- 34 B. Li, Z. Tian, L. Li, Y. H. Wang, Y. Si, H. Wan, J. Shi, G. F. Huang, W. Hu, A. Pan and W. Q. Huang, *ACS Nano*, 2023, **17**, 3465–3482.
- 35 W. He, R. Zhang, H. Liu, Q. Hao, Y. Li, X. Zheng, C. Liu, J. Zhang and H. L. Xin, *Small*, 2023, **19**, 2301610.
- 36 S. Lee, M. R. Ashwin Kishore, D. Kim, H. Kang, J. Chun, L. S. Oh, J. H. Park, H. J. Kim, J. S. Yoo and E. Lim, *ACS Appl. Energy Mater.*, 2022, **5**, 14658–14668.
- 37 G. Gao, Y. Jiao, E. R. Waclawik and A. Du, *J. Am. Chem. Soc.*, 2016, **138**, 6292–6297.
- 38 Y. Li, B. Li, D. Zhang, L. Cheng and Q. Xiang, *ACS Nano*, 2020, **14**, 10552–10561.
- 39 X. Liu, W. Yang, L. Chen, Z. Liu, L. Long, S. Wang, C. Liu, S. Dong and J. Jia, *ACS Appl. Mater. Interfaces*, 2020, **12**, 4463–4472.
- 40 R. Shen, J. Xie, Y. Ding, S. Y. Liu, A. Adamski, X. Chen and X. Li, *ACS Sustain. Chem. Eng.*, 2019, **7**, 3243–3250.
- 41 S. Mousavi-Salehi, S. Keshipour and F. Ahour, *J. Phys. Chem. Solids*, 2023, **176**, 111239.
- 42 X. Zou, X. Huang, A. Goswami, R. Silva, B. R. Sathe, E. Mikmeková and T. Asefa, *Angew. Chemie*, 2014, **126**, 4461–4465.
- 43 B. R. Sathe, X. Zou and T. Asefa, *Catal. Sci. Technol.*, 2014, **4**, 2023–2030. DOI: 10.1039/D4YA00463A
- 44 S. S. Narwade, S. M. Mali, R. V. Digraskar, V. S. Sapner and B. R. Sathe, *Int. J. Hydrogen Energy*, 2019, **44**, 27001–27009.
- 45 V. S. Sapner, P. P. Chavan, A. V. Munde, U. S. Sayyad and B. R. Sathe, *Energy and Fuels*, 2021, **35**, 6823–6834.
- 46 Y. Li, Y. Wang, C. L. Dong, Y. C. Huang, J. Chen, Z. Zhang, F. Meng, Q. Zhang, Y. Huangfu, D. Zhao, L. Gu and S. Shen, *Chem. Sci.*, 2021, **12**, 3633–3643.
- 47 L. Liu, S. Du, X. Guo, Y. Xiao, Z. Yin, N. Yang, Y. Bao, X. Zhu, S. Jin, Z. Feng and F. Zhang, *J. Am. Chem. Soc.*, 2022, **144**, 2747–2754.
- 48 Y. Liu and Z. Xiang, *ACS Appl. Mater. Interfaces*, 2019, **11**, 41313–41320.
- 49 G. Wang and Z. Jin, *ChemistrySelect*, 2019, **4**, 3602–3610.
- 50 L. Lu, Q. Li, R. Zhang, J. Jiang, S. Zhang, J. Guo, P. Cheng and W. Shi, *ACS Appl. Energy Mater.*, 2023, **6**, 8072–8080.
- 51 F. Yang, S. Huang, B. Zhang, L. Hou, Y. Ding, W. Bao, C. Xu, W. Yang and Y. Li, *Nanomaterials*, 2019, **9**, 1022.
- 52 S. Shanmugam, A. Sivanantham, M. Matsunaga, U. Simon and T. Osaka, *Electrochim. Acta*, 2019, **297**, 749–754.
- 53 S. Sirisomboonchai, S. Li, A. Yoshida, S. Kongparakul, C. Samart, Y. Kansha, X. Hao, A. Abudula and G. Guan, *Catal. Sci. Technol.*, 2019, **9**, 4651–4658.
- 54 J. R. N. dos Santos, I. C. B. Alves, A. L. B. Marques and E. P. Marques, *Electrocatalysis*, 2022, **13**, 713–730.
- 55 S. S. Yu, T. H. Lee and T. H. Oh, *Fuel*, 2022, **315**, 123151.
- 56 M. Mahiuddin and B. Ochiai, *ACS Omega*, 2022, **7**, 35626–35634.
- 57 B. T. Hoan, P. D. Tam and V. H. Pham, *J. Nanotechnol.*, 2019, **2019**, 2852816.
- 58 A. Tadesse, M. Hagos, D. Ramadevi, K. Basavaiah and N. Belachew, *ACS Omega*, 2020, **5**, 3889–3898.
- 59 T. K. Mondal, A. Gupta, B. K. Shaw, S. Mondal, U. K. Ghorai and S. K. Saha, *RSC Adv.*, 2016, **6**, 59927–59934.
- 60 E. M. Schneider, A. Bärtsch, W. J. Stark and R. N. Grass, *J. Chem. Educ.*, 2019, **96**, 540–545.
- 61 F. Ortega, V. B. Arce and M. A. Garcia, *Carbohydr. Polym.*, 2021, **252**, 117208.
- 62 M. A. Marwat, M. Humayun, M. W. Afridi, H. Zhang, M. R. Abdul Karim, M. Ashtar, M. Usman, S. Waqar, H. Ullah, C. Wang and W. Luo, *ACS Appl. Energy Mater.*, 2021, **4**, 12007–12031.
- 63 A. Anantha Krishnan, A. K. Aneesh, R. B. Nair, R. Sivaraj, A. Lamiya, P. K. Jishnu, S. Kurian, T. Mathew, M. Ameen Sha and P. S. Arun, *New J. Chem.*, 2022, **46**, 22256–22267.
- 64 S. S. Mani, S. Rajendran, N. Nalajala, T. Mathew and C. S. Gopinath, *Energy Technol.*, 2022, **10**, 1–12.
- 65 D. Ahmadkhaniha, F. Eriksson and C. Zanella, *Coatings* 2020, Vol. 10, Page 1179, 2020, **10**, 1179.
- 66 Y. Zhang, X. Hou, X. Li, D. Li, F. Huang and Q. Wei, *J. Colloid Interface Sci.*, 2020, **578**, 805–813.
- 67 X. Cheng, J. Zheng, J. Li and X. Luo, *ChemistrySelect*, 2019, **4**, 4271–4277.
- 68 P. Bazant, I. Kuritka, L. Munster and L. Kalina, *Cellulose*, 2015, **22**, 1275–1293.



- 69 M. C. Biesinger, L. W. M. Lau, A. R. Gerson and R. S. C. Smart, *Phys. Chem. Chem. Phys.*, 2012, **14**, 2434–2442.
- 70 Y. Wei, Z. Han, T. Liu, X. Ding and Y. Gao, *Chem. Commun.*, 2023, **59**, 11572–11575.
- 71 P. Córdoba-Torres, T. J. Mesquita and R. P. Nogueira, *J. Phys. Chem. C*, 2015, **119**, 4136–4147.
- 72 S. Anantharaj, P. E. Karthik and S. Noda, *Angew. Chemie*, 2021, **133**, 23235–23251.
- 73 M. Mathankumar, S. Anantharaj, A. K. Nandakumar, S. Kundu and B. Subramanian, *J. Mater. Chem. A*, 2017, **5**, 23053–23066.
- 74 M. Ledendecker, S. Krickalderöñ, C. Papp, H. P. Steinrück, M. Antonietti and M. Shalom, *Angew. Chemie Int. Ed.*, 2015, **54**, 12361–12365.
- 75 Y.-H. Wang, L. Li, J. Shi, M.-Y. Xie, J. Nie, G.-F. Huang, B. Li, W. Hu, A. Pan, W.-Q. Huang, Y.-H. Wang, L. Li, J. Shi, M.-Y. Xie, J. Nie, G.-F. Huang, B. Li, W.-Q. Huang, W. Hu and A. Pan, *Adv. Sci.*, 2023, **10**, 2303321.
- 76 F. Song, M. M. Busch, B. Lassalle-Kaiser, C. S. Hsu, E. Petkucheva, M. Bensimon, H. M. Chen, C. Corminboeuf and X. Hu, *ACS Cent. Sci.*, 2019, **5**, 558–568.
- 77 N. Danilovic, R. Subbaraman, D. Strmcnik, K. C. Chang, A. P. Paulikas, V. R. Stamenkovic and N. M. Markovic, *Angew. Chemie Int. Ed.*, 2012, **51**, 12495–12498.
- 78 L. Yang, Y. Wu, F. Wu, Y. Zhao, Z. Zhuo, Z. Wang, X. Li, Y. Luo and J. Jiang, *J. Mater. Chem. A*, 2020, **8**, 20946–20952.
- 79 P. Chandrasekharan Meenu, P. K. Samanta, T. Yoshida, N. J. English, S. P. Datta, S. A. Singh, S. Dinda, C. Chakraborty and S. Roy, *ACS Appl. Energy Mater.*, 2022, **5**, 503–515.
- 80 G. F. Chen, T. Y. Ma, Z. Q. Liu, N. Li, Y. Z. Su, K. Davey and S. Z. Qiao, *Adv. Funct. Mater.*, 2016, **26**, 3314–3323.
- 81 A. A. Krishnan, H. Sreehari, M. A. A. Kumar, R. B. Nair, S. Kurian, M. A. Sha and P. S. Arun, *Catal. Sci. Technol.*, , DOI:10.1039/D4CY00627E.
- 82 S. Khatun, S. Pal and P. Roy, *J. Alloys Compd.*, 2024, **977**, 173393.
- 83 K. Srinivas, Y. Chen, B. Wang, B. Yu, Y. Lu, Z. Su, W. Zhang and D. Yang, *ACS Appl. Mater. Interfaces*, 2020, **12**, 55782–55794.
- 84 C. Huang, J. Zhou, D. Duan, Q. Zhou, J. Wang, B. Peng, L. Yu and Y. Yu, *Chinese J. Catal.*, 2022, **43**, 2091–2110.
- 85 H. Fei, J. Dong, Y. Feng, C. S. Allen, C. Wan, B. Voloskiy, M. Li, Z. Zhao, Y. Wang, H. Sun, P. An, W. Chen, Z. Guo, C. Lee, D. Chen, I. Shakir, M. Liu, T. Hu, Y. Li, A. I. Kirkland, X. Duan and Y. Huang, *Nat. Catal.* 2018 **11**, 2018, **1**, 63–72.
- 86 I. han Yoo, S. S. Kalanur and H. Seo, *Appl. Catal. B Environ.*, 2019, **250**, 200–212.
- 87 D. Gao, W. Liu, Y. Xu, P. Wang, J. Fan and H. Yu, *Appl. Catal. B Environ.*, 2020, **260**, 118190.
- 88 R. Purbia and S. Paria, *Dalt. Trans.*, 2017, **46**, 890–898.

View Article Online
DOI: 10.1039/D4YA00463A



From,

View Article Online
DOI: 10.1039/D4YA00463A

Arun P S
Corresponding author
arunps@stjohns.ac.in

To,
The Editor
Energy Advances

Dear Sir,

The data that support the finding of the study titled “Ag-NiP Deposited Green Carbon Channels Embedded NiP Panels for Sustainable Water Splitting “are available from the corresponding author, upon reasonable request.

Thank You.
Arun, P. S.

